Discover Oncology

RESEARCH Open Access

Characterization and regulatory mechanism evaluation of C8orf33 in hepatocellular carcinoma through multiomics profiling

Wei Gao[1,2,3†], Siyi Xing[4†], Mingjiang Liu[1,2,3], Xing Xie[5], Mei Feng[5], Zhipeng Quan[1,2,3], Housheng Wang[2,3,6], Zhilong He[2,3,6], Qianxin Hu[2,3,6], Huizhao Su[1,2,3], Shuiping Yu[1,2,3*] and Zeyuan Li[1,2,3*]

[†]Wei Gao and Siyi Xing have contributed equally to this work.

*Correspondence:
Shuiping Yu
yushuiping03@163.com
Zeyuan Li
lizeyuan03@126.com

Full list of author information is available at the end of the article

Abstract

Background Hepatocellular carcinoma (HCC) is a major cause of cancer-related mortality. Chromosome 8 open reading frame 33 (C8orf33) has been noted as a potential oncogenic factor in several cancers, but its biological roles and regulatory mechanism in HCC microenvironment remain unknown.

Methods We integrated bulk RNA sequencing, single-cell RNA sequencing (scRNA-seq), and spatial transcriptomics (ST) to characterize the expression landscape of C8orf33. We then performed C8orf33 loss-of-function studies in HCC cell lines, including in vitro phenotypic assays and subcutaneous xenografts.

Results C8orf33 was broadly overexpressed and associated with unfavorable prognosis across multiple Cancers. In HCC, higher C8orf33 aligned with advanced stage and shorter overall survival. C8orf33 knockdown reduced proliferation and migration, impaired tumorigenic capacity, and increased apoptosis. ScRNA-seq analyses identified a malignant population of Epi3 with high C8orf33 expression. Cell–cell communication analysis suggested that C8orf33-high Epi3 state was associated with an enriched MIF–CD74/CXCR4/CD44 signaling program toward macrophage populations with M2-like features. ST analyses further confirmed the colocalization of C8orf33 with malignant features in tumor cores. In Huh7 cells, C8orf33 knockdown was accompanied by reduced mRNA and protein levels of MIF and its receptor components. Consistently, xenografts derived from C8orf33-silenced cells showed lower expression of these MIF-axis components and reduced infiltration of CD163 and CD206-positive macrophages.

Conclusion These results support a tumor-promoting association of C8orf33 in HCC and suggest a potential link to macrophage-associated immunomodulatory features, nominating C8orf33 as a candidate biomarker and therapeutic target.

Keywords Hepatocellular carcinoma, C8orf33, Single-cell RNA-seq, Spatial transcriptomics, MIF signaling pathway

1 Introduction

HCC is a major global health problem and is the third leading cause of cancer-related death worldwide [1]. Around 80% of cases occur in regions with less developed or moderately developed health-care systems, with a particular concentration in East Asia and sub-Saharan Africa [2]. HCC is a multifactorial disease. Chronic infection with hepatitis B virus (HBV) or hepatitis C virus (HCV) has long been the dominant driver, but its etiologic profile is now shifting. The rising prevalence of metabolic dysfunction-associated steatotic liver disease and its inflammatory phenotype is fueling a new wave of HCC incidence, especially in Western populations and urbanized regions [3, 4]. Despite advances in surveillance, a large proportion of patients are still diagnosed at intermediate or advanced stages, when curative treatment is no longer possible.

The current medical therapy of advanced HCC has reached a therapeutic plateau. Transarterial chemoembolization (TACE) remains the standard treatment for intermediate-stage disease [5]. For advanced-stage HCC, available options now include molecular targeted agents and immune checkpoint inhibitors (ICIs) [6, 7]. The recent development of ICIs, such as the medicine atezolizumab combined with bevacizumab, provided a novel standard of therapy. However, efficacy of such treatments is poor, as evidenced by objective response rate persisting under 35% [8]. This poor efficacy can be attributed to the fundamentally biological phenomenon of HCC, whereby malignant hepatocytes repattern the tumor microenvironment to exclude cytotoxic T lymphocytes and maintain the immunosuppressed microenvironment [9, 10]. It is, thus, a pertinent task to elucidate the molecular interactions of tumor sub-clones and the immune microenvironment to look for fresh targets for therapy that can break this immune tolerance.

C8orf33 is located on human chromosome 8q24.3, a region frequently amplified in multiple cancers. C8orf33 expression is upregulated by genetic copy number amplification and by epigenetic mechanisms of DNA hypomethylation. Previous work has linked high C8orf33 expression to tumor progression and poor clinical prognosis in breast cancer [11]. Moreover, C8orf33 was found to be connected to the management of DNA repair from oncogene-driven replication stress in head and neck carcinoma, where this was observed to be linked to head and neck squamous cell carcinoma [12]. Studies in osteosarcoma further suggest that C8orf33 modulates replication stress pathways, including ATR–CHK1 signaling, and contributes to treatment resistance while creating an opportunity for PARP inhibitor–based strategies [13]. However, its role in HCC is still largely unclear. Even though initial bioinformatical analyses suggested that poor differentiation and high tumor load of HCC was linked to C8orf33 expression, numerous other works need to be elucidated to determine its comprehensive implications [14, 15]. It remains unknown whether C8orf33 acts merely as a passive marker of genomic instability or as an active orchestrator of tumor progression and immune evasion.

Moving from correlation to mechanism requires resolution beyond traditional bulk genomic profiling, which averages signals across heterogeneous tumor clones and can obscure rare but aggressive subpopulations [16, 17]. We therefore used scRNA-seq and ST to examine the role of C8orf33 in HCC. We found that C8orf33 is associated with enhanced malignant phenotypes and is linked to immune microenvironment. A malignant epithelial subset (Epi3) with high C8orf33 expression shows an enriched MIF–CD74/CXCR4 communication signature with macrophage subsets, suggesting a potential link to M2-like polarization states. Together, these observations suggest that

C8orf33-high malignant states may be associated with proliferative imbalance and macrophage-associated immunomodulation.

2 Materials and methods

2.1 Acquisition of data

These publicly available data sets have been systematically collected for a multi-omics investigation. The pan-cancer (Table.S1) transcriptome data, clinical phenotypes, and tumor mutational burdens (TMB) were obtained from the UCSC Xena browser platform(http://xena.ucsc.edu/), where TCGA(https://cancergenome.nih.gov/) and GTEx (https://www.gtexportal.org/home/)cohorts have been integrated. Proteomic pro files for C8orf33 across tumors were accessed via the CPTAC dataset (https://cprosite.ccr.cancer.gov/) through the cProSite portal [18]. For single-cell analysis, scRNA-seq data comprising healthy, adjacent non-tumor, borderline, and tumor tissues were compiled from four GEO datasets (GSE189903, GSE151530, GSE115469, and GSE185477). Rigorous quality control was performed: cells with < 200 detected features or > 20% mitochondrial gene content were excluded, yielding a final dataset of 232,905 high-quality cells. Raw sequencing data for serial ST sections (HCC1–HCC4), covering non-tumor (N), leading-edge (L), and tumor (T) regions, have been deposited in the Genome Sequence Archive for Human (GSA-Human) under accession number HRA000437.

2.2 Tissue specimens and clinical samples

Stored paired HCC and adjacent non-tumor liver tissue ($n = 8$ pairs) were collected from patients with hepatocellular carcinoma who underwent radical resection at the First Affiliated Hospital of Guangxi Medical University by previous researchers. All patients were free of hepatitis B virus or hepatitis C virus infection and had not received chemotherapy, radiotherapy, or immunotherapy prior to surgery. All subjects signed informed consent forms before surgery. This study protocol was approved by the Ethics Committee of the First Affiliated Hospital of Guangxi Medical University (Approval No.: 2025-E0508; June 18, 2025) and conducted in accordance with the principles of the Declaration of Helsinki.

2.3 Pan-cancer differential expression and prognostic analysis of C8orf33

Subcellular localization and protein abundance of C8orf33 were verified using the Human Protein Atlas (HPA). Associations between C8orf33 transcript levels and survival endpoints as well as clinical stage were assessed by logistic regression and univariate Cox proportional-hazards models implemented with the R packages "limma", "survival", and "survminer". The samples were stratified into cohorts of high and low expression using the cohort mean as the cut-off point. Diagnostic and prognostic performance was summarized by receiver operating characteristic (ROC) analyses using the "pROC" package [19].

2.4 Immunological correlation analysis

TMB and MSI scores were retrieved from TCGA's database. Spearman's rank correlation analysis was performed to investigate the correlations of C8orf33 expression with TMB and MSI. The P values and correlation coefficients generated were visually presented in the form of radar charts with the "fmsb" R package [20]. The correlation of C8orf33

expression and other immune features was analyzed using the "limma" and "CIBERSORT" software tools [21].

2.5 Expression and clinical prognostic significance of C8orf33 in HCC

In order to validate the expression and prognostic value of C8orf33 specifically in HCC, data from TCGA-LIHC and six independent GEO cohorts (GSE14520, GSE25097, GSE12148, GSE54536, GSE64041, and GSE89377) were analyzed. C8orf33 expression levels were correlated with clinicopathologic variables, including histological grade, age, sex, and TNM stage. Heatmaps visualizing these correlations were generated using the "ComplexHeatmap" package. Multivariate Cox regression analysis was performed to identify independent prognostic factors, which were then integrated to construct a nomogram for predicting 1, 3, and 5-year overall survival (OS) using the "rms" and "regplot" packages.

2.6 scRNA-seq and functional analysis

scRNA-seq data were processed using the Seurat (v4.3.0) [22]and Harmony (v1.2.0) [23]. Top 2,000 variable genes were applied for PCA and batch correction (PC1–PC50) using Harmony after normalization. Clustering was performed using a K-nearest neighbor graph (K = 20) and was resolution optimized (0.1–2.0) using clustree (v0.5.1) [24]. Cell type specific marker genes were identified via the application of Seurat's FindAllMarkers function (log2FC > 0.25, min.pct > 0.25) [22]. For visualization, Uniform Manifold Approximation and Projection (UMAP) embeddings were generated. Cell identities were assigned by integrating canonical lineage markers with the ScType algorithm [25] and the Annotation of Cell Types (ACT) resource [26]. Major populations (parenchymal, myeloid, lymphoid, stromal) were identified, followed by subset analysis. Tumor cells within parenchymal clusters were inferred using inferCNV (v1.18.1) [27]. 6 parenchymal, 10 myeloid, and 11 lymphoid subsets were identified. Differential expression analysis was performed using the Wilcoxon test on genes expressed in > 25% of Tumor-Epi 3 cells (adjusted $P < 0.05$, $|\log2FC| > 0.585$), with visualization using plot1cell (v0.0.0.9000) [28]. Functional enrichment analysis with the Kyoto Encyclopedia of Genes and Genomes (KEGG) pathways and ontology (GO) terms were performed using clusterProfiler (v4.10.1) [29] and GSVA (v1.50.1) [30], with visualization by GseaVis (v0.0.5) and pheatmap (v1.0.12). Epithelial trajectory analysis was conducted with Monocle2 (v2.30.0) [31], using healthy cells as the guide, and was visualized through ClusterGVis (v0.1.2) [32].

2.7 Cell–cell communication analysis

The CellChat (v1.6.1) [33] package was used to infer cell–cell interactions between subsets of tumor parenchymal cells and immune cells. Ligand–receptor pairs with $P < 0.05$ were considered for downstream analysis and visualization.

2.8 Spatial transcriptomics analysis

We used the R Seurat (v5.2.1) [22] and harmony (v1.2.3) [23] packages to integrate the expression data from different sections of HCC1/HCC2/HCC3 and HCC4 patients and used the R SPATA2 (v3.1.3) [34] package to perform the basic downstream analysis. The

R shiny (v1.10.0) [35] package was used to manually segment the tumor regions from the slices of the ST.

2.9 Cell culturing and gene transfection

Human HCC cell lines SNU-449, LM3, MHCC97H, MIHA, SNU-182, and Huh-7 were obtained from the American Type Culture Collection (ATCC). Cells were cultured in DMEM or RPMI-1640 (Gibco, USA) medium with 10% fetal bovine serum (FBS; Gibco, USA) and 1% penicillin-streptomycin (P1400, Solarbio, China). The cultures were kept in an incubator at 37 °C in a humidified atmosphere of 5% CO2. All cell lines underwent routine mycoplasma testing for verification of their mycoplasma contamination absence. shRNA plasmid (SnapGene, USA) targeting C8orf33 was transfected into cells by Lipofectamine 3000 (L3000001; Invitrogen, USA) following the guidelines of the manufacturer.

2.10 Cell proliferation assays

For the Cell Counting Kit-8 (CCK-8) assay, cells were seeded at a density of 1,000 cells/well in 96-well plates. Following incubation, CCK-8 reagent (Dojindo, Japan) was added, and cells were incubated for 2 h. Then the absorbance was measured at 450 nm using a BioTek microplate reader. For 5-ethynyl-2'-deoxyuridine (EdU) assays, cells were labeled using the EdU Cell Proliferation Kit (Beyotime, China) and counterstained with Hoechst. Images were captured using an Olympus IX71 microscope, and each condition was examined in triplicate. For the colony formation assays, 500 cells were plated into 6-well plates and their culture was maintained for 14 days. When colonies became visible, they were fixed with 4% paraformaldehyde, stained, and photographed to permit counting.

2.11 Cellular cycle and apoptosis analysis

Cells were harvested 48 h post-transfection. For cell cycle analysis, cells were stained using the Cell Cycle Staining Kit (Liankebio, China) followed by flow cytometric analysis. Apoptosis was evaluated using the Annexin V-APC/7-AAD Apoptosis Detection Kit (Liankebio, China) according to the manufacturer's instructions.

2.12 RNA isolation and quantitative real-time PCR

Total RNA was extracted using RNAiso Plus reagent (Takara, Japan). First-strand cDNA synthesis was conducted using RT Mix (RR036A, Takara, Japan). PCR was performed with qPCR mix (RR047A, Takara, Japan) on a CFX96™ Real-Time PCR System (Bio-Rad, USA). The primer sequences are listed in Supplementary Table 2.

2.13 Western blotting and antibody information

Total protein was extracted via RIPA lysis buffer supplemented with PMSF, and concentrations were quantified using the BCA assay (P0006C, Beyotime, China). Protein samples were resolved by SDS–PAGE and transferred onto PVDF membranes. Following blocking with 5% non-fat milk, membranes were incubated overnight at 4 °C with primary antibodies against C8orf33 (1:500, bs-15286R, Bioss), MIF (1:1000, A22623, ABclonal), CD74 (1:1000, A26945PM, ABclonal), CD44 (1:2000, A28567PM, ABclonal), CXCR4 (1:500, 60042-1-Ig, Proteintech)and β-actin (1:10,000, 20536-1-AP, Proteintech).

Membranes were then incubated with HRP-conjugated goat anti-rabbit secondary antibodies (1:5,000, SA00001-2, Proteintech), and bands were visualized using the LI-COR imaging system.

2.14 Immunohistochemistry

Fresh tumor tissues were formalin-fixed, dehydrated, and paraffin-embedded. Five-micrometer sections were treated with citrate buffer (pH 6.0) for antigen retrieval and blocked for endogenous peroxidase activity. The tissue sections were then incubated overnight at 4 °C with primary antibodies against C8orf33 (1:100, bs-15286R, Bioss), MIF (1:100, A22623, ABclonal), CD44 (1:500, A28567PM, ABclonal), CXCR4 (1:400, 60042-1-Ig, Proteintech), CD206 (1:2,000, 18704-1-AP, Proteintech), and CD163 (1:1,000, 16646-1-AP, Proteintech). After the washing step, the sections were processed for staining using a biotinylated secondary antibody (PV-6000, ZSGB-Bio, China) and developed using DAB (ZSGB-Bio, China). Subsequently, hematoxylin counterstaining of the tissue sections was performed, and these sections were mounted and analyzed under a biological microscope. Quantitative evaluation of staining was performed using the ImageJ (NIH, USA) platform, where color deconvolution was applied to distinguish the background hematoxylin from the developed DAB. Percentage positivity was measured by determining the percentage of tissue area positive for DAB.

2.15 Immunofluorescence staining

After deparaffinization, rehydration, and antigen retrieval (EDTA buffer, pH 9.0). Sections were then permeabilized, blocked and incubated overnight at 4 °C with an anti-CD74 primary antibody (1:500; A26945PM, ABclonal), followed by an Alexa Fluor 594–conjugated secondary antibody (1:1000; RGAR004; Proteintech). Nuclei were counterstained with DAPI. Images were captured via fluorescence microscopy, and relative expression was quantified in ImageJ as the ratio of the target mean fluorescence intensity to the DAPI intensity.

2.16 Animal studies

Male BALB/c nude mice (6 weeks old) were procured from the Laboratory Animal Center of Guangxi Medical University. Following an acclimatization period, the mice were randomized into experimental groups. The animal study protocol was approved by the Animal Ethics Committee of the First Affiliated Hospital of Guangxi Medical University (Approval No. 202503007; June 23, 2025). The maximal tumor size permitted by the ethics committee was 1.5 cm in diameter, and we confirm that this limit was not exceeded in any experiments. To establish the xenograft model, Huh7 cells were harvested during the logarithmic growth phase and resuspended in sterile PBS to create a single-cell suspension. A volume of 100 μL containing the cells was subcutaneously inoculated into the flank of the mice. Tumor dimensions were monitored weekly. At the study endpoint (4 weeks post-inoculation), animals were anesthetized using isoflurane inhalation and subsequently euthanized via cervical dislocation. The subcutaneous tumors were excised, weighed, and photographed. Finally, the tumor tissues were fixed in 4% paraformaldehyde for downstream pathological evaluation.

2.17 Statistical analysis

All analyses were done by R version 4.5.0, SPSS version 26.0, or GraphPad Prism version 9.5.0. When making comparisons between two different groups, we performed unpaired t-tests or Wilcoxon rank-sum tests. When making comparisons among scores of more than two groups, we performed one-way ANOVA. Correlation tests, such as Pearson correlation test or Spearman correlation test, were done according to the data distributions. All experiments had triplicates, and each was done at least thrice. $^{*}P < 0.05$; $^{**}P < 0.01$; $^{***}P < 0.001$.

3 Results

3.1 C8orf33 is aberrantly expressed and prognostically significant across multiple cancers

To systematically determine the oncogenic potential of C8orf33, we conducted a comprehensive pan-cancer analysis. Evaluations of TCGA, GTEx, and CPTAC datasets showed that transcripts and protein expression of C8orf33 was significantly elevated across a range of carcinomas compared to corresponding normal tissue expression levels (Fig. 1A–C, Fig. S1A). By using logistic regression and univariate Cox proportional hazard models, high C8orf33 expression was associated with poorer survival outcomes across multiple cancer type (Fig. 1D, Fig. S1B–D). Additionally, ROC curve analyses indicated that C8orf33 expression showed good discriminatory performance for distinguishing tumor from corresponding non-tumor tissues across datasets (Fig. S1E). Correlation analyses further showed that C8orf33 expression was significantly associated with genomic instability markers (TMB, MSI) and immune infiltration patterns (Fig. 1E–H), suggesting a potential link between C8orf33 and the tumor immune microenvironment across cancers.

3.2 Elevated C8orf33 associates with aggressive clinicopathologic features and unfavorable prognosis in HCC

Based on the strong C8orf33 deregulation found within our pan-cancer screen, validation analyses concentrated on HCC. Consistent with the initial findings, C8orf33 mRNA was markedly overexpressed in HCC tissues compared to adjacent non-tumor liver tissues across the TCGA-LIHC cohort (Fig. 2A) and validated in six independent GEO datasets (Fig. 2B). Besides, its protein expression was confirmed to be highly upregulated within HCC tissues by immunohistochemical staining of the clinical tissue specimens (Fig. 2C). ROC analysis confirmed its robust discriminatory efficacy for HCC diagnosis (Fig. 2D). Clinically, high C8orf33 expression was significantly associated with male sex and advanced histological stages (Fig. 2E), though not with age (Fig. 2F). Kaplan-Meier curves demonstrated that the high-C8orf33 group had significantly reduced overall survival (OS) and disease-free interval (DFI) (Fig. 2G). Univariate and multivariable Cox models showed that C8orf33 (HR = 1.456, $P = 0.007$) and clinical stage independently predicted overall survival (Fig. 2H–I). Based on these findings, we established a nomogram integrating C8orf33 with standard clinical parameters, which demonstrated high concordance between predicted and actual 1-, 3-, and 5-year survival rates (Fig. 2J).

3.3 C8orf33 knockdown impairs HCC tumorigenicity in vitro and in vivo

To investigate the biological function of C8orf33, we screened a panel of HCC cell lines, Huh-7 cells exhibited the highest endogenous expression levels and were consequently

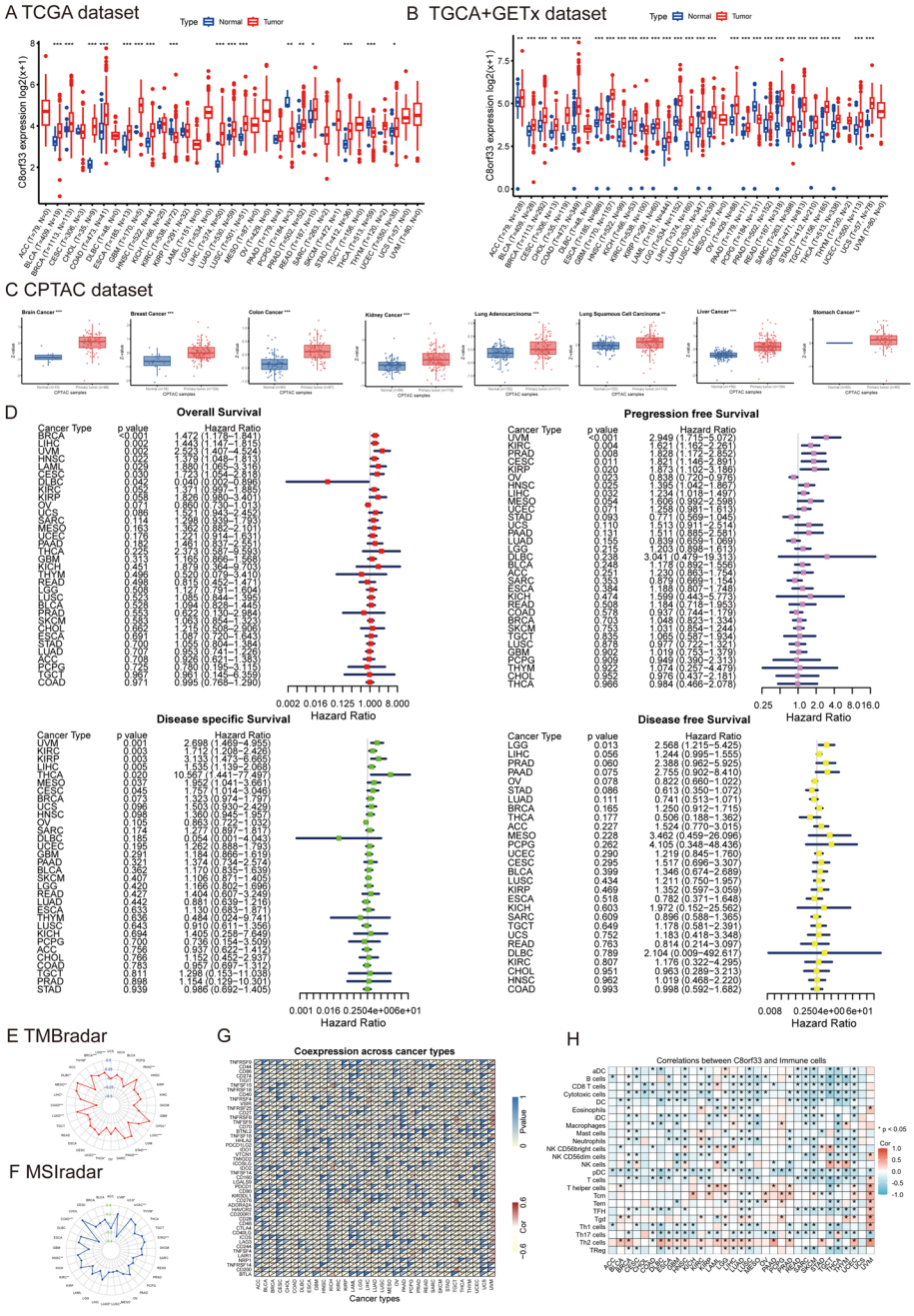

Fig. 1 Pan-Cancer Analysis Reveals C8orf33 as a Broadly Upregulated Oncogene Candidate with Prognostic Significance. (A) Analysis of C8orf33 mRNA expression levels across 33 tumor types using TCGA data. (B) Differential expression of C8orf33 mRNA in tumor and normal tissues, integrating data from the GTEx and TCGA databases. (C) Proteomic analysis of C8orf33 abundance in normal versus tumor tissues across multiple cancer types (brain, breast, colon, kidney, lung, and liver) using the CPTAC dataset. (D) Forest plot showing univariate Cox proportional hazards regression analysis of the prognostic value of C8orf33 across various cancers in the TCGA database. (E–F) Radar charts illustrating the correlation between C8orf33 expression and Tumor Mutation Burden (TMB) (E) and Microsatellite Instability (MSI) (F). (G) Heatmap displaying the co-expression patterns of C8orf33 with immune-related genes across diverse tumor types. (H) Heatmap summarizing links between C8orf33 abundance and levels of immune-cell infiltration. Bars indicate mean ± SD. *$P < 0.05$; **$P < 0.01$; *** $P < 0.001$

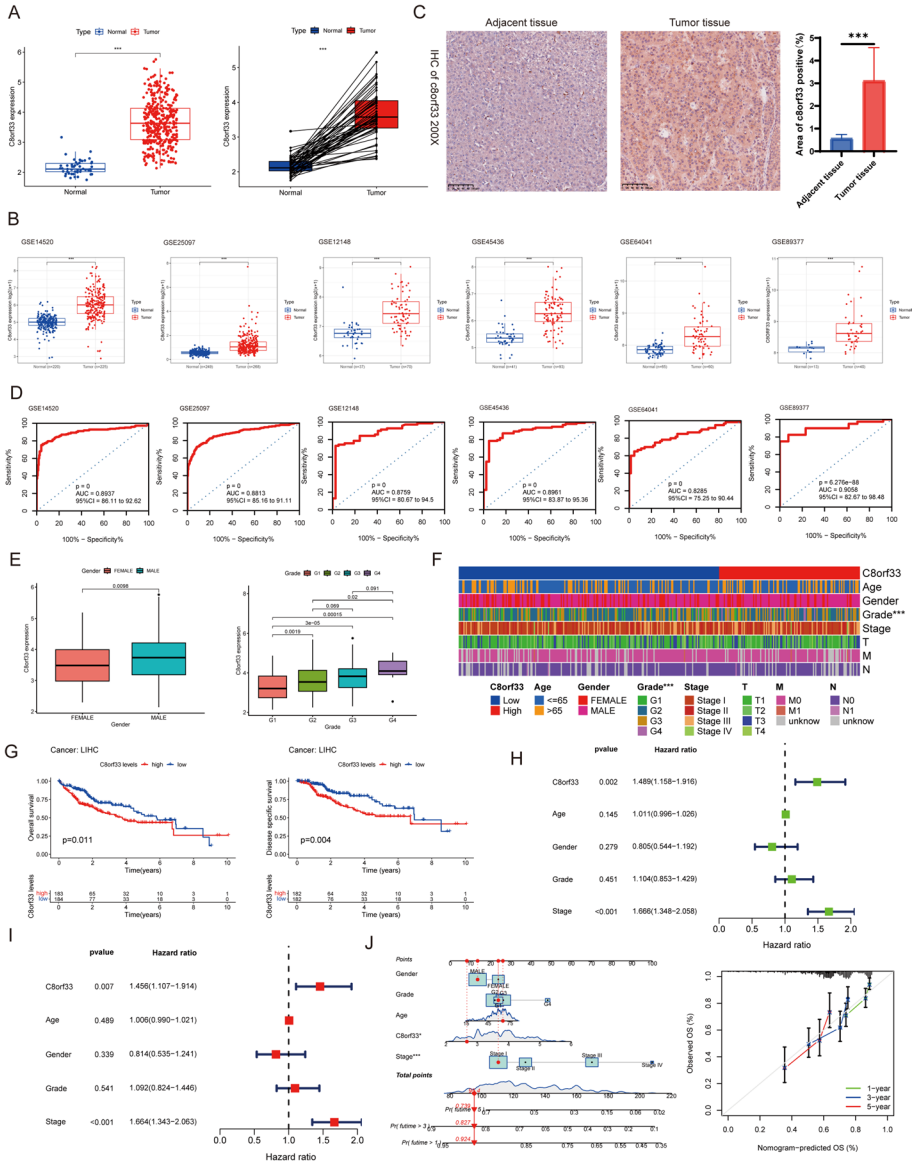

Fig. 2 High C8orf33 expression is associated with aggressive clinicopathologic characteristics and unfavorable prognosis in HCC. (A) Comparison of C8orf33 mRNA levels between HCC tumors and adjacent non-tumor liver tissues in the TCGA-LIHC cohort. (B) Validation of C8orf33 mRNA upregulation in HCC using six independent GEO datasets (GSE14520, GSE25097, GSE12148, GSE45436, GSE64041, and GSE89377).(C) Representative immunohistochemistry (IHC) images showing C8orf33 protein abundance in adjacent non-tumor and HCC tissues ($n = 8$/group). 200×,Scale bar, 100 μm. (D) Receiver Operating Characteristic (ROC) curves assessing the diagnostic performance of C8orf33 in the six GEO datasets. (E) Boxplots depicting relationships between C8orf33 expression and clinical features, including sex and pathological stage. (F) Heatmap visualizing the correlation between C8orf33 expression and clinicopathologic variables. (G) Kaplan-Meier survival curves evaluating Overall Survival (OS) and Disease-Specific Survival (DSS) based on C8orf33 expression levels. (H, I) Univariate (H) and Multivariate (I) Cox regression analyses identifying independent prognostic factors in HCC. (J) Prognostic nomogram combining C8orf33 expression with clinical stage, with calibration plots demonstrating agreement between predicted and observed 1-, 3-, and 5-year survival. All values are expressed as the means ± SD, * $P < 0.05$; ** $P < 0.01$; *** $P < 0.001$

selected as the optimal model for loss of function assays (Fig. 3A). We established stable knockdown models using shRNA targeting C8orf33. Knockdown efficiency was confirmed by qRT-PCR and Western blotting; C8orf33-sh1 exhibited the most robust suppression and was selected for subsequent experiments (Fig. 3B). Downregulation of C8orf33 significantly attenuated malignant phenotypes of HCC cells. In vitro, In

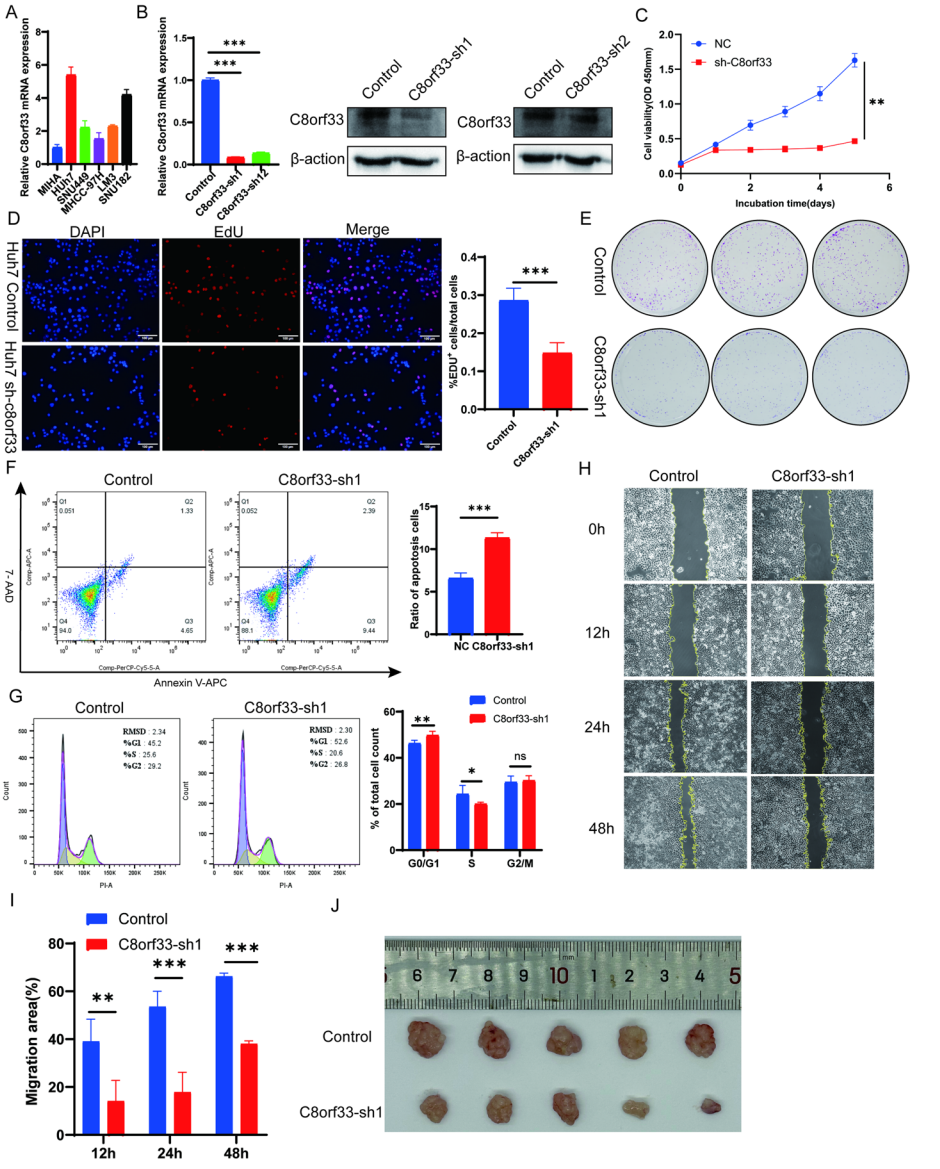

Fig. 3 C8orf33 Knockdown Impairs HCC Tumorigenicity and Progression In Vitro and In Vivo (A) RT-qPCR screening of C8orf33 basal expression in an immortalized hepatocyte line (MIHA) and five HCC cell lines (Huh-7, LM3, SNU-449, MHCC-97 H, SNU-182). (B) Validation of shRNA-mediated knockdown efficiency in Huh-7 cells via Western blotting and RT-qPCR. (C) CCK-8 assay measuring time-dependent changes in cell viability following C8orf33 knockdown. (D) EdU incorporation assay. Representative images and quantification of EdU-positive cells (EdU+/total nuclei). Scale bar, 100 μm. (E) Representative images of colony formation assays.(F)Flow cytometric analysis of apoptosis rates using Annexin V/PI staining. (G) Flow cytometric analysis of cell cycle distribution. (H, I) Wound healing assay(H) and quantitative analysis (I) of cell migration capabilities. (J) Representative images of subcutaneous xenograft tumors excised from nude mice. All values are expressed as the mean ± SD, *P < 0.05, **P < 0.005, ***P < 0.001

vitro, C8orf33 knockdown significantly reduced proliferative capacity, evidenced by a markedly slower increase in CCK-8 signal over time and decreased EdU incorporation (Fig. 3C–D). Colony-forming ability was also impaired (Fig. 3E). Flow cytometric analyses revealed that knockdown of C8orf33-induced G0/G1 cell-cycle arrest and a significantly increased rate of apoptosis (Fig. 3F–G). Wound migration assays showed that knockdown of C8orf33 significantly reduced the migration ability of HCC cells (Fig. 3H–I). Finally, our subcutaneous xenograft models confirmed that knockdown of C8orf33

significantly suppressed tumor growth, as evidenced by reduced tumor sizes compared to controls (Fig. 3J). Overall, these findings support a tumor-promoting role of C8orf33 in HCC models and indicate that C8orf33 contributes to proliferation, survival, migration, and xenograft growth.

3.4 Single-cell profiling identifies a C8orf33-high malignant "Epi3" subpopulation

To examine how C8orf33 relates to cellular heterogeneity in HCC, we integrated scRNA-seq data from four public cohorts that included healthy liver, adjacent tissue, border regions, and tumor cores. After quality control and batch correction, cells were grouped into four major compartments: parenchymal, myeloid, lymphoid, and stromal (Fig. 4A). The proportions of these cell types differed across tissue sources (Fig. 4B–D), and immune cells infiltrated all non-healthy samples. Cell identities were assigned based on canonical marker genes (Fig. S2A-B). Focusing on the tumor parenchyma, we reclustered hepatocytes into six subpopulations: Epi1–4, KRT7$^+$ cholangiocyte-like cells (CHO), and FXYD2$^+$ CHO (Fig. 4E). Spatial mapping showed distinct distribution patterns, with Epi3 markedly enriched in tumor core regions (Fig. 4F–H; Fig. S2C). inferCNV analysis revealed widespread chromosomal copy number alterations in all six tumor-derived parenchymal clusters compared with healthy controls, consistent with malignant transformation (Fig. 4I). Among these clusters, C8orf33 expression was notably higher in Epi2 and Epi3 (Fig. 4J, Fig. S2D).

We next placed these populations along a developmental axis using pseudotime trajectory analysis. The trajectory suggested a bifurcation from healthy epithelium into two main branches: a maintenance branch ending in Epi2 and a malignant progression branch ending in Epi3 (Fig. 4K). Along the branch toward Epi3, C8orf33 expression increased, whereas differentiation markers such as DHCR24 and ALDH4A1 declined (Fig. 4L). To characterize the C8orf33-high Epi3 state, we performed enrichment analyses (Fig. S3). GO and KEGG results indicated that Epi3 cells are metabolically active and proliferative, with enrichment of ribosome biogenesis, RNA splicing, p53 signaling, and oxidative phosphorylation (Fig. S3A–D). GSEA supported enhanced protein synthesis and energy metabolism (Fig. S3E–F). GSVA suggested partial overlap of malignant-associated programs between the tumor Epi3 state and Epi1 (Fig. S3G). Importantly, the C8orf33-high Epi3 population was predominantly enriched in tumor core regions and localized to the terminal segment of the progression branch in the pseudotime trajectory. These results suggest that C8orf33-high Epi3 may represents a dedifferentiated malignant state with enhanced metabolic and biosynthetic programs, rather than simply reflecting a higher-expression continuum of Epi1.

3.5 C8orf33-high Epi3 cells exhibit enhanced mif signaling interactions with M2-like macrophages

Having identified C8orf33-high Epi3 parenchymal cells as a key malignant subset, we next examined their relationship with the tumor immune microenvironment. We reclustered myeloid cells into ten subtypes: M2-like macrophages (M2-like MCs), SEPP1$^+$CCL3L3$^+$ MCs, FABP4$^+$FABP5$^+$ MCs, type 2 dendritic cells (DCs), type 1 DCs, CD5L$^+$MARCO$^+$ MCs, classical monocytes (Mos), tumor-associated macrophages (TAMs), nonclassical Mos, and neutrophils (Fig. 5A). Myeloid composition varied across tissue regions, with M2-like macrophages showing marked accumulation around the

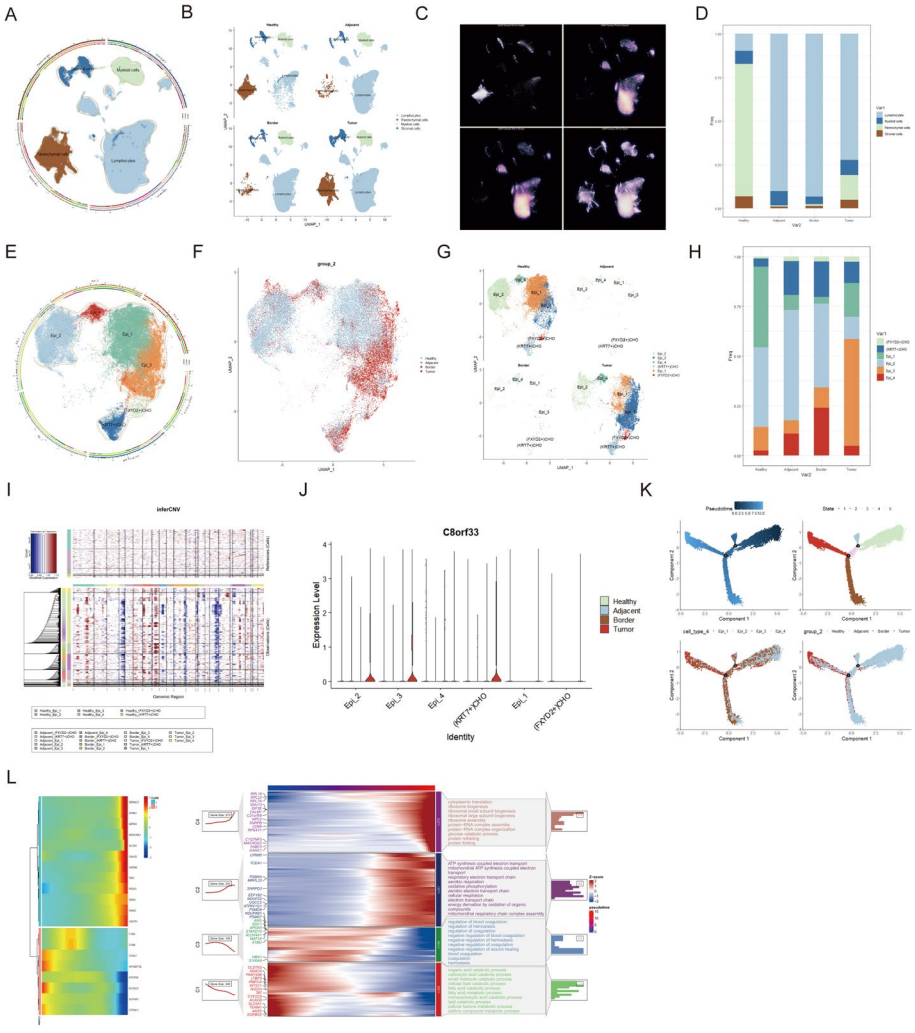

Fig. 4 Single-Cell Transcriptomics Delineates a High-C8orf33 Malignant Trajectory Characterized. (A) Global UMAP projection of 232,905 single cells, annotated by major lineages: parenchymal cells, myeloid cells (MCs), lymphocytes, and stromal cells. (B) UMAP plot colored by tissue origin (Healthy, Adjacent, Border, Tumor). (C, D) density plot (C) and Stacked bar plot (D) illustrating the proportional distribution and density of cell lineages across different sample types. (E) UMAP visualization of 34,622 re-clustered parenchymal cells, identifying six subpopulations: Epi1–4, (KRT7+) CHO, and (FXYD2+) CHO. (F) UMAP plot of parenchymal cells colored by tissue source, highlighting spatial heterogeneity.(G) Split UMAP visualization showing the distribution of parenchymal subpopulations across different tissue types. (H) Stacked bar plot showing the composition of parenchymal subpopulations in each sample group. (I) Heatmap of inferred chromosomal copy number variations (CNVs), distinguishing malignant cells from normal hepatocytes. (J) Violin plots showing C8orf33 expression levels across different parenchymal subpopulations. (K) Pseudotime trajectory analysis of epithelial differentiation, inferring a transition from normal to malignant states. (L) Heatmap modeling dynamic gene expression changes and enriched pathways along the epithelial differentiation trajectory

tumor core (Fig. 5B, C). CellChat was then used to map ligand–receptor communication within the TME. M2-like macrophages emerged as major hubs, acting as both prominent signal receivers and senders (Fig. 5D).

Focusing on C8orf33-high Epi3 cells, we analyzed their outgoing interactions with myeloid lineages. Among the predicted ligand–receptor pairs, the macrophage migration inhibitory factor (MIF) pathway ranked among the top communication signals between Epi3 cells and M2-like macrophages (Fig. 5E). Epi3 cells also signaled through additional pathways, including CD99 (Fig. 5F), while M2-like macrophages integrated

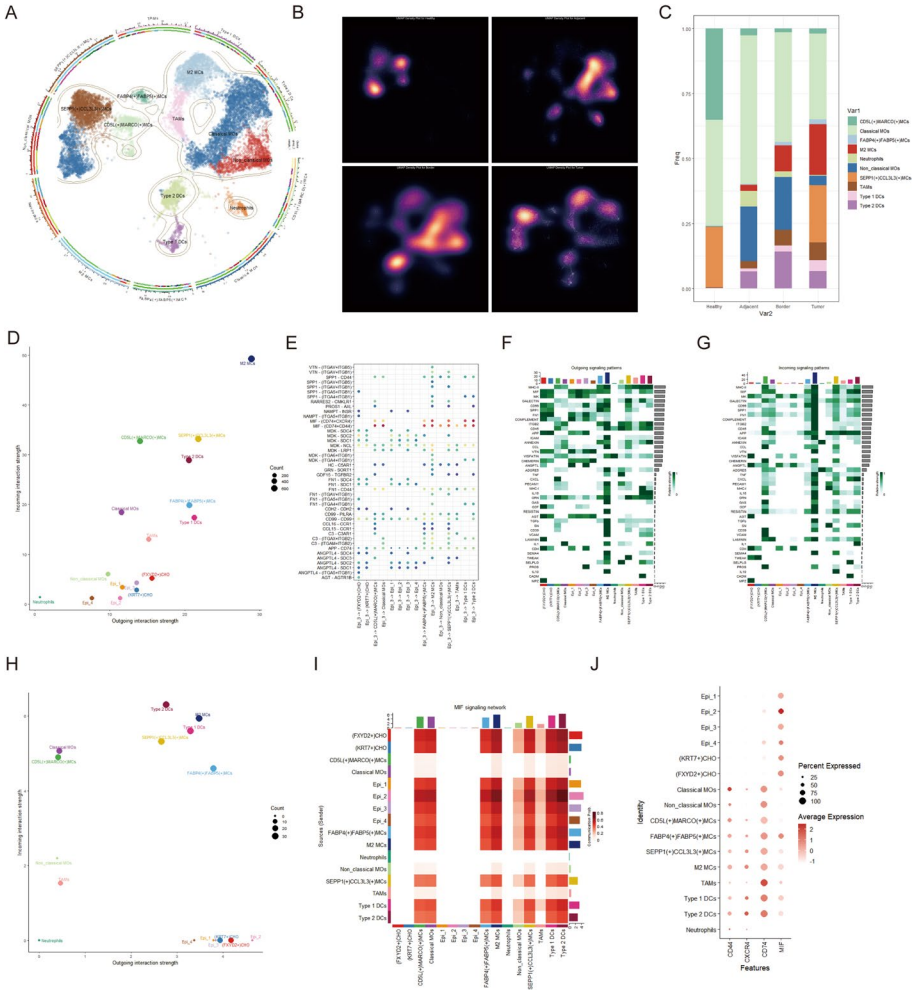

Fig. 5 Cell Chat Inference Highlights MIF Signaling from C8orf33-high Epi3 Cells to M2-like Macrophage. (A) UMAP visualization of 15,086 re-clustered myeloid cells, annotated into 10 subtypes: M2-like MCs, SEPP1(+) CCL3L3(+) MCs, FABP4(+) FABP5(+) MCs, Type 2 DCs, Type 1 DCs, CD5L(+)MARCO(+)MCs, classical Mos, TAMs, non-classical Mos, neutrophils. (B) Density plot comparing myeloid cell distribution across Healthy, Adjacent, Border, and Tumor Core tissues. (C) Stacked bar plot showing the relative proportion of myeloid subsets in different samples. (D) Network diagram illustrating the major predicted senders and receivers of intercellular signaling between parenchymal and myeloid cells.(E) Ligand-receptor interaction bubble plot showing significant signaling pairs between the malignant Epi3 subpopulation and distinct myeloid subsets. (F, G) Heatmaps displaying the contribution of specific signaling pathways to the outgoing (F) and incoming (G) signaling patterns of parenchymal and myeloid cells. (H, I) Scatter plot (H) and heatmap (I) summarizing the inferred communication strength of the MIF signaling pathway. (J) Dot plot showing the expression patterns of MIF ligand in tumor cells and its receptors in myeloid cells

multiple inputs such as complement-related signaling (Fig. 5G). Analysis of the MIF network showed that parenchymal cells were the main senders in this pathway, whereas myeloid cells were the principal receivers (Fig. 5H-I). Concordantly, MIF was highly expressed in Epi3 tumor cells, and its receptors CD74, CXCR4, and CD44 were enriched in M2-like macrophages (Fig. 5J). Signaling from Epi3 cells was also associated with altered lymphocyte infiltration patterns (Fig. S4). These analyses support an association between the C8orf33-high Epi3 state and an enriched MIF–CD74/CXCR4/CD44 communication signature with macrophage subsets displaying M2-like features.

3.6 Spatial transcriptomics reveals C8orf33 enrichment in tumor regions

To examine the spatial heterogeneity observed through scRNA-seq, we analyzed spatial transcriptomics data from four HCC patients, including peritumoral, boundary, and tumor regions. Across all four spatial transcriptomic datasets, C8orf33 expression was consistently higher in tumor regions than in adjacent areas (Fig. 6A–D). Among them, the HCC-4 boundary sample exhibited the most distinct tumor–non-tumor difference and was selected for downstream spatial analyses (Fig. 6D). H&E staining of the HCC-4 boundary section enabled clear delineation of tumor versus non-tumor areas (Fig. 6E). Consistent with this annotation, established tumor markers (e.g., KRT7) showed higher expression in the tumor area, further supporting the regional classification (Fig. 6F). To quantify these spatial differences, we performed manual region segmentation using an interactive Shiny-based workflow (Fig. 6G). This analysis showed that C8orf33 expression was elevated in the tumor compartment relative to the non-tumor compartment (Fig. 6H). GSEA of differentially expressed genes indicated that the C8orf33-high tumor compartment was enriched for oncogenic signaling pathways, including mTOR, p53, and Wnt signaling pathways (Fig. 6I).

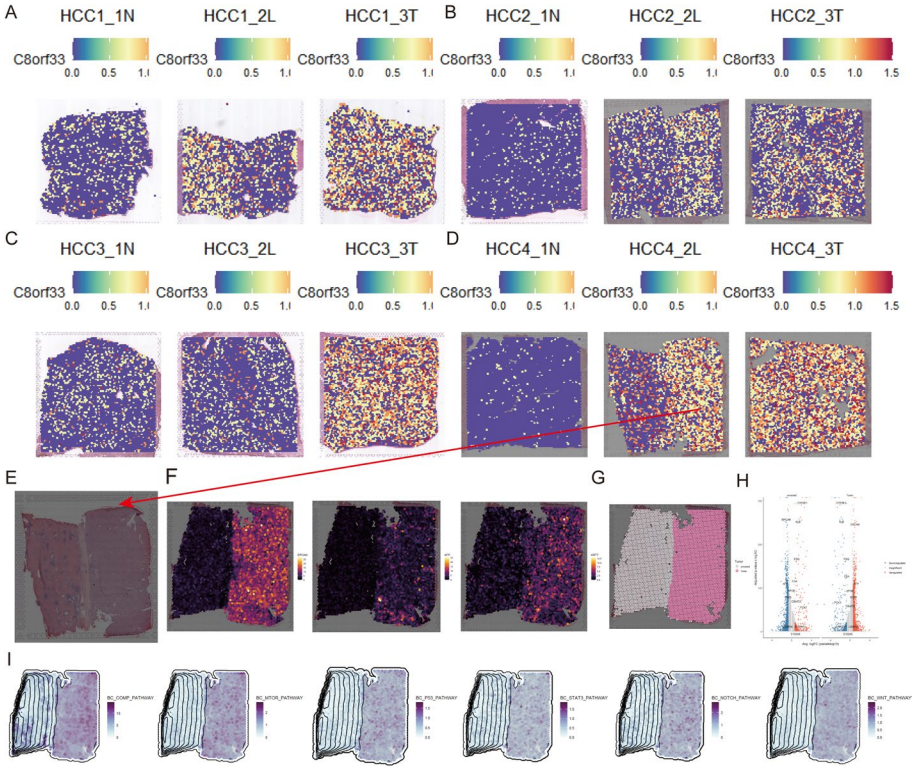

Fig. 6 Spatial transcriptomics reveals C8orf33 enrichment in the tumor core and tumor edge. (A-D) Spatial feature plots visualizing C8orf33 expression across Adjacent Normal (N), Tumor Edge (L), and Tumor Center (T) regions in four HCC patients (HCC1–HCC4). (E) H&E staining of the boundary section from patient HCC-4. (F) Spatial expression of canonical markers (EPCAM, AFP, KRT7) in the HCC-4 boundary section. (G) Visualization of manually segmented tumor and non-tumor regions using an interactive Shiny-based workflow. (H) Volcano plot identifying differentially expressed genes between the segmented tumor and non-tumor regions in HCC-4. (I) GSEA results summarizing enrichment of oncogenic signaling pathways in the tumor region relative to the non-tumor region of HCC-4

3.7 C8orf33 knockdown reduces MIF-axis components and M2-like macrophage infiltration

To experimentally evaluate the C8orf33–MIF–macrophage relationship suggested by our omics analyses, we assessed MIF-axis components at both the transcript and protein levels in xenograft tumor tissues derived from C8orf33-knockdown versus control Huh-7 cells. RT–qPCR showed that C8orf33 knockdown was accompanied by reduced mRNA expression of MIF and its receptors (CD74, CD44, and CXCR4) (Fig. 7A). Consistently, WB confirmed reduced protein levels of MIF, CD74, CD44, and CXCR4 following C8orf33 knockdown (Fig. 7B).

We then performed histological analyses to localize these changes and to assess macrophage infiltration in xenograft tumors. IHC demonstrated decreased staining of MIF, CD44, and CXCR4 in tumors derived from C8orf33-knockdown cells compared with controls (Fig. 7C), and IF further showed reduced CD74 signal in the knockdown group (Fig. 7D). In parallel, IHC staining for macrophage markers revealed a reduced positive area of CD163 and CD206 in C8orf33-knockdown xenografts, suggesting reduced infiltration of M2-like macrophage (Fig. 7E). In clinical specimens, CD163 and CD206 staining was higher in HCC tissues than in matched adjacent non-tumor tissues, consistent with enrichment of M2-like macrophage features in the HCC microenvironment (Fig. 7F). Collectively, these findings support an association between C8orf33 expression and elevated expression of MIF-axis components, together with increased M2-like macrophage features in HCC.

4 Discussion

HCC remains a major clinical challenge worldwide. Its marked biological heterogeneity and intricate immune landscape collectively limit the efficacy of current immunotherapies [36]. C8orf33, located within the 8q24 amplicon, is often regarded as a passenger gene co-amplified with MYC [15, 37]. Although C8orf33 dysregulation in cancer has been reported [15], its precise role in tumor progression remains unclear. Through multi-omics profiling and functional experiments, we found C8orf33 is highly expressed in HCC and associated with unfavorable prognosis. The nomogram incorporating C8orf33 achieves good concordance for survival prediction, suggesting that this marker may refine current prognostic systems and help identify patients at higher risk. Furthermore, we identified a C8orf33-high malignant Epi3 subpopulation that communicates with M2-like macrophages via the MIF-CD74/CD44/CXCR4 signaling axis. Collectively, these findings challenge the conventional view of C8orf33 as a bystander and highlight its critical role in promoting tumor progression and modulating the tumor microenvironment.

C8orf33 is an evolutionarily conserved protein-coding gene on human chromosome 8. Its encoded protein belongs to the UPF0488 family and contains a highly conserved DUF4615 domain whose function remains incompletely understood [38]. Available evidence suggests that C8orf33 may act as a factor integrating genome integrity with metabolic homeostasis in hepatocytes. Bishara et al. reported that C8orf33 antagonizes KAT8 acetyltransferase activity and maintains relatively low H4K16ac in quiescent hepatocytes, which helps restrict aberrant homologous recombination and preserve genome stability in polyploid hepatocytes [38–41]. In addition, C8orf33 is regulated by gluconeogenesis inhibitors and one-carbon metabolism fluctuations, serving as a downstream target

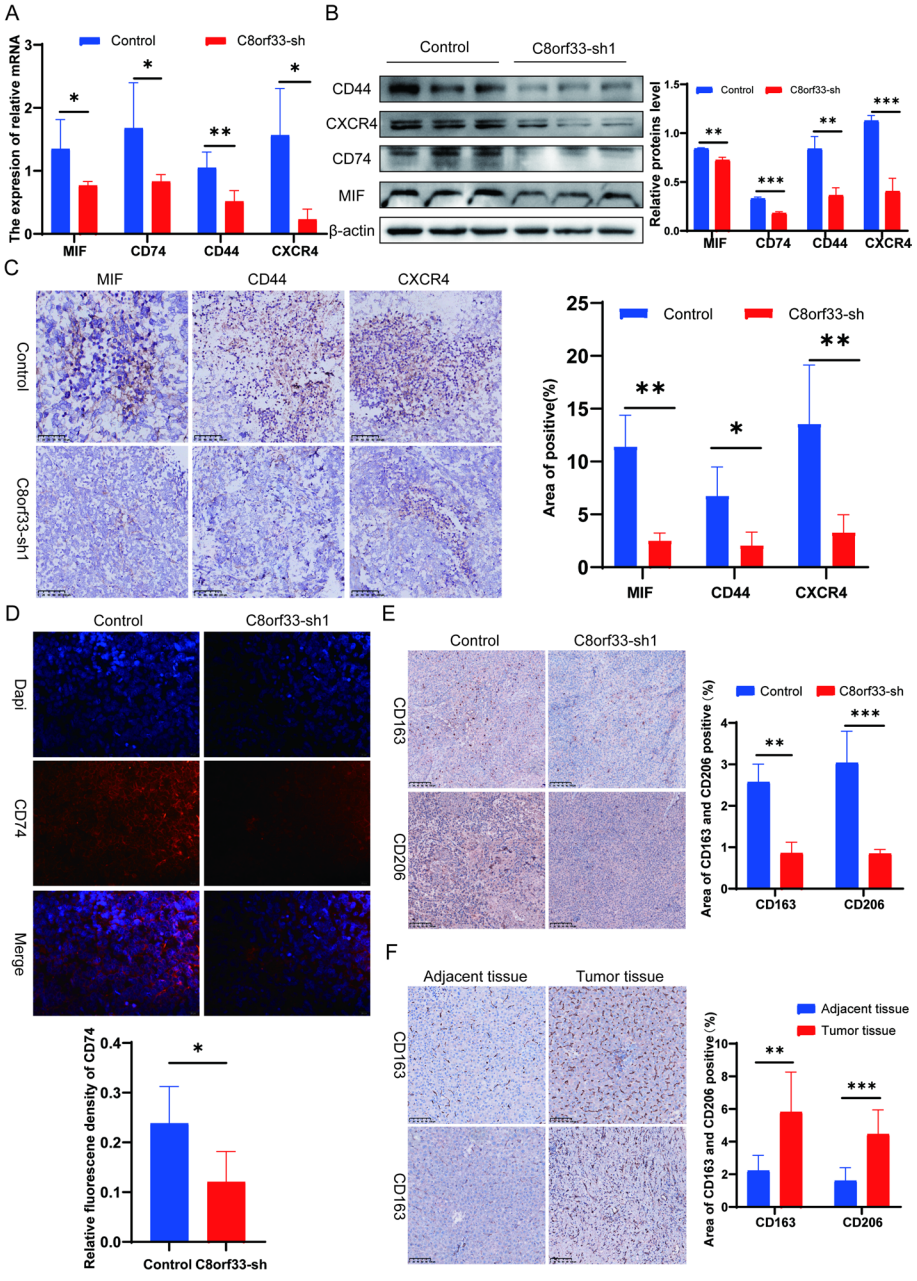

Fig. 7 C8orf33 knockdown reduces MIF-axis components and M2-like macrophage infiltration. (A) RT–qPCR analysis of MIF-axis components (MIF, CD74, CD44, and CXCR4) in xenograft tumor tissues derived from control (sh-NC) and C8orf33-knockdown (sh-C8orf33) Huh-7 cells. (B) WB analysis of MIF, CD74, CD44, and CXCR4 protein expression in xenograft tumor tissues from sh-NC and sh-C8orf33 groups and quantification. (C) IHC staining of MIF, CD44, and CXCR4 in xenograft tumors, with quantification ($n = 5$ per group). 200×; scale bar, 100 μm. (D) Immunofluorescence staining of CD74 in xenograft tumors, with quantification ($n = 5$ per group). 400×; scale bar, 50 μm. (E) Representative IHC images of CD163 and CD206 and quantification of positive staining area in xenograft tumors derived from sh-NC and sh-C8orf33 groups ($n = 5$ per group). 200×; scale bar, 100 μm. (F) Representative IHC images of CD163 and CD206 and quantification of positive staining area in adjacent non-tumor and HCC tissues ($n = 8$ per group). 200×; scale bar, 100 μm. The values are shown as the means ± SDs. *$P < 0.05$; **$P < 0.01$; ***$P < 0.001$

of ATF4 in integrated stress responses [42, 43]. This facilitates coordinated chromatin remodeling to adapt to energy states and protects hepatocytes from protein toxicity or genotoxic damage [44]. Based on these roles, its dysregulation may lead to hyperplasia and provide abundant energy, contributing to tumorigenesis and progression.

Our multi-omics analysis revealed C8orf33's potential role in regulating the tumor microenvironment. Single-cell sequencing showed significant upregulation of C8orf33 in tumor epithelial cell subpopulations along the trajectory from normal hepatocytes to tumor cells. Notably, this tumor-Epi3 subpopulation exhibited the highest proportion in tumor tissues, demonstrated pronounced malignant characteristics, and was associated with extensive copy number variations. Gene set enrichment analysis further indicated that pathways associated with rapid proliferation and metabolism—such as translation, ribosome biosynthesis, and oxidative phosphorylation—were significantly enriched in the C8orf33-high tumor-Epi3 subpopulation. This suggests that C8orf33 overactivation may confer tolerance to genomic stress from amplification and other lesions while providing sufficient energy for amplification [38]. Concurrently, immune-related pathways (complement activation, neutrophil trap formation, and iron dysregulation) also showed an upward trend, suggesting that C8orf33 dysregulation may also impact the tumor microenvironment. These findings were indirectly corroborated by our in vitro experiments: C8orf33 knockdown weakened hepatocellular carcinoma cell proliferation, increased apoptosis, and induced G0/G1 phase arrest. Collectively, C8orf33 dysregulation may induce DNA damage tolerance and supply energy for rapid proliferation, though deeper validation remains necessary.

Beyond its potential intrinsic role, our multi-omics analysis suggests C8orf33 may also influence the tumor microenvironment, thereby affecting tumor progression. Cell communication analysis indicates that the MIF signaling pathway is significantly enriched in the core region of HCC tumors. Tumor epithelial cells serve as the primary signal senders, with C8orf33-high tumor Epi 3 cells exhibiting stronger cell communication intensity, while M2-like macrophages are the main signal recipients. Prior studies have suggested that heightened ribosome biogenesis and stress responses can influence inflammatory mediator expression and release, including MIF [45, 46]. And MIF binds to CD74/CXCR4 receptors on macrophage surfaces, driving their recruitment and polarization toward the M2-like phenotype [47]. Besides, some studies indicate that M2-like macrophages in the tumor microenvironment can promote immunosuppression by releasing inhibitory cytokines and PD-L1, while also facilitating angiogenesis and invasion through vascular endothelial growth factor production and matrix remodeling [48, 49]. Tissue analysis from C8orf33-knockdown Huh7 cell xenograft models revealed decreased mRNA and protein expression of MIF and its ligands CD74/CD44/CXCR4, along with reduced M2-like macrophage infiltration. In summary, the cellular communication between C8orf33-high tumor Epi 3 cells and M2-like macrophages may mediate immune environment alterations in the tumor microenvironment, thereby promoting tumor progression. However, the underlying mechanisms driving these changes require further investigation.

Understanding the role of C8orf33 in tumors holds therapeutic implications, particularly for HCC immunotherapy. Limited clinical response to ICIs in some HCC patients stems partly from the highly complex tumor immune microenvironment [50]. Our study suggests that increased MIF secretion following C8orf33 dysregulation may act on M2-like macrophages, altering the tumor microenvironment and promoting tumor progression. Inhibiting C8orf33 may simultaneously disrupt tumor cell proliferation homeostasis and energy supply while altering the tumor microenvironment through M2-like macrophage infiltration. This opens possibilities for testing MIF pathway inhibitors or

C8orf33-targeting drugs in combination with current PD-1/PD-L1 blockers. However, we must recognize its fundamental role as an evolutionarily conserved gene in normal liver physiology. As previously described, it is crucial for preventing abnormal homologous recombination and maintaining polyploid genome stability, while also playing a role in energy metabolism. Therefore, when evaluating the safety of C8orf33 as a therapeutic target, consideration must be given to the potential disruption of normal liver epigenetic homeostasis and weakened capacity to respond to metabolic stress caused by long-term inhibition of this gene.

Several limitations warrant acknowledgment. First, our current analysis relies on public data and requires validation in larger, independent clinical cohorts. Second, although the findings suggest an association between C8orf33 and the MIF axis, the absence of experiments involving C8orf33 overexpression or MIF rescue limits causal inference. Third, in vivo studies utilized immunodeficient nude mouse xenograft models, precluding assessment of immunological consequences in immunocompetent settings. Finally, the physiological function of C8orf33 in normal hepatocytes and potential off-target toxicity require further evaluation. Future studies combining immunocompetent models, more refined analysis of tumor-associated macrophage subtypes, and rescue experiments will further elucidate the potential mechanisms by which C8orf33 promotes hepatocellular carcinoma and assesses therapeutic feasibility.

5 Conclusion

In summary, our study demonstrates that C8orf33 is upregulated in HCC and is associated with adverse clinical outcomes. Integrated scRNA-seq and spatial transcriptomics analyses identify a C8orf33-high malignant epithelial state (Epi3) enriched in tumor core regions. Multi-omics inference and functional validation further support an association between C8orf33 expression, increased MIF-axis signaling components, and M2-like macrophage features in HCC. These findings suggest that C8orf33 may serve as a prognostic biomarker and a candidate target for future investigations aimed at modulating tumor-intrinsic programs and macrophage-associated immunomodulation in HCC.

Abbreviations

C8orf33	Chromosome 8 open reading frame 33
DFI	Disease-free interval
DSS	Disease-specific survival
GTEx	The Genotype-Tissue Expression
HCC	Hepatocellular carcinoma
HPA	The Human Protein Atlas
ICIs	immune checkpoint inhibitors
MIF	The macrophage migration inhibitory factor
MSI	Microsatellite instability
OS	Overall survival
PFI	Progression-free interval
ROC	Receiver operating characteristic
ScRNA-seq	Single-cell RNA-sequencing
ST	Spatial transcriptome
TAM	Tumor-associated macrophage
TMB	Tumor mutation burden
TCGA	The Cancer Genome Atlas
UCSC	The University of California Santa Cruz

Supplementary Information

The online version contains supplementary material available at https://doi.org/10.1007/s12672-026-04951-z.

Supplementary Material 1.

Supplementary Material 2.

Supplementary Material 3.

Acknowledgements
We thank LetPub (www.letpub.com.cn) for its linguistic assistance during the preparation of this manuscript.

Author contributions
W.G., SY.X. and MJ.L. designed and guided the study, conducted experiments, wrote the manuscript. X.X. and M.F. conducted experiments and designed the figures. ZP. Q. and HS.W. helped conduct animal experiments. ZL.H and QX.H assisted with drawing and writing the manuscript. HZ. S, SP. Y, and ZY. L. designed and supervised the study. All authors reviewed and approved the manuscript.

Funding
This work was supported by Joint Project on Regional High-Incidence Diseases Research of Guangxi Natural Science Foundation (2025GXNSFAA069021,2023GXNSFAA026001); National Natural Science Foundation of China (82360515); Youth Science Foundation of Guangxi Medical University (GXMUYSF202414).

Data availability
The datasets analysed during the current study are available in public repositories. Specifically, the single-cell RNA sequencing (scRNA-seq) datasets (Accession Nos. GSE189903, GSE151530, GSE115469, and GSE185477) and bulk RNA-seq datasets (Accession Nos. GSE14520, GSE25097, GSE12148, GSE54536, GSE64041, and GSE89377) were retrieved from the Gene Expression Omnibus (GEO) database([https://www.ncbi.nlm.nih.gov/geo/](https:/www.ncbi.nlm.nih.gov/geo)). The raw spatial transcriptomics sequencing data analysed in this study have been deposited in the Genome Sequence Archive for Human (GSA-Human) under accession number HRA000437 ([https://ngdc.cncb.ac.cn/gsa-human/browse/HRA000437](https:/ngdc.cncb.ac.cn/gsa-human/browse/HRA000437)). Additionally, pan-cancer transcriptome data from the TCGA([https://cancergenome.nih.gov/](https:/cancergenome.nih.gov)) and GTEx ([https://www.gtexportal.org/home/](https:/www.gtexportal.org/home)) cohorts were accessed via the UCSC Xena browser ([http://xena.ucsc.edu/](http:/xena.ucsc.edu)), and proteomic profiles were retrieved from the CPTAC dataset via the cProSite portal ([https://cprosite.ccr.cancer.gov/](https:/cprosite.ccr.cancer.gov)).Any additional data supporting the findings of this study are available from the corresponding author upon reasonable request.

Declarations

Ethics approval and consent to participate
The collection and use of human clinical specimens were conducted in accordance with the Declaration of Helsinki (as revised in 2013). The study protocol was approved by the Ethics Committee of the First Affiliated Hospital of Guangxi Medical University (Approval No. 2025-E0508; June 18, 2025). The animal study protocol was approved by the Animal Ethics Committee of the First Affiliated Hospital of Guangxi Medical University (Approval No. 202503007; June 23, 2025). The animal experiments were conducted in accordance with the Guide for the Care and Use of Laboratory Animals prepared by the National Academy of Sciences and published by the National Institutes of Health (NIH Publication 86 – 23, revised 1985). This guideline permits the inclusion of mice with tumor sizes up to 1.5 cm in maximal diameter. We confirm that the maximal tumor burden was maintained below 5% of the animal's total body weight in all experimental subjects, and these limits were not exceeded. Informed consent was obtained from all patients for the collection and use of their tissue samples.

Consent for publication
All authors have agreed to the publication of this manuscript.

Competing interests
The authors declare no competing interests.

Author details
[1]Guangxi Key Laboratory of Immunology and Metabolism for Liver Diseases, the First Affiliated Hospital of Guangxi Medical University, No. 6 Shuangyong Road, Nanning 530021, Guangxi, China
[2]Division of Hepatobiliary Surgery, The First Affiliated Hospital of Guangxi Medical University, Nanning 530021, Guangxi, China
[3]Key Laboratory of Early Prevention and Treatment for Regional High Frequency Tumor, Guangxi Medical University, Ministry of Education, Nanning 530021, Guangxi, China
[4]School of Life Science, Hubei University, Wuhan 430062, Hubei, China
[5]Clinical Laboratory Center, The First Affiliated Hospital of Guangxi Medical University, Nanning 530021, China
[6]Department of Radiation Oncology, The First Affiliated Hospital of Guangxi Medical University, Nanning 530021, Guangxi, China

Received: 9 December 2025 / Accepted: 2 April 2026
Published online: 11 April 2026

References

1. Tang W, Sun G, Ji G-W, Feng T, Zhang Q, Cao H, et al. Single-cell RNA-sequencing atlas reveals an FABP1-dependent immunosuppressive environment in hepatocellular carcinoma. J Immunother Cancer. 2023;11:e007030. https://doi.org/10.1136/jitc-2023-007030.

2. Peng B, Quan Z, Liang L, Liu M, Hu K, Chen S, et al. The LncRNA lnc-POTEM-4:14 promotes HCC progression by interacting with FOXK1. Sci Rep. 2025;15:7672. https://doi.org/10.1038/s41598-025-92614-4.
3. Huang Y, Xie Y, Zhang Y, Liu Z, Jiang W, Ye Y, et al. Single-cell transcriptome reveals the reprogramming of immune microenvironment during the transition from MASH to HCC. Mol Cancer. 2025;24:177. https://doi.org/10.1186/s12943-025-02370-2.
4. Yang JD, Hainaut P, Gores GJ, Amadou A, Plymoth A, Roberts LR. A global view of hepatocellular carcinoma: trends, risk, prevention and management. Nat Rev Gastroenterol Hepatol. 2019;16:589–604. https://doi.org/10.1038/s41575-019-0186-y.
5. Llovet JM, De Baere T, Kulik L, Haber PK, Greten TF, Meyer T, et al. Locoregional therapies in the era of molecular and immune treatments for hepatocellular carcinoma. Nat Rev Gastroenterol Hepatol. 2021;18:293–313. https://doi.org/10.1038/s41575-020-00395-0.
6. Cheng A-L, Qin S, Ikeda M, Galle PR, Ducreux M, Kim T-Y, et al. Updated efficacy and safety data from IMbrave150: atezolizumab plus bevacizumab vs. sorafenib for unresectable hepatocellular carcinoma. J Hepatol. 2022;76:862–73. https://doi.org/10.1016/j.jhep.2021.11.030.
7. Finn RS, Qin S, Ikeda M, Galle PR, Ducreux M, Kim T-Y, et al. Atezolizumab plus bevacizumab in unresectable hepatocellular carcinoma. N Engl J Med. 2020;382:1894–905. https://doi.org/10.1056/NEJMoa1915745.
8. Qin S, Chan SL, Gu S, Bai Y, Ren Z, Lin X, et al. Camrelizumab plus rivoceranib versus sorafenib as first-line therapy for unresectable hepatocellular carcinoma (CARES-310): a randomised, open-label, international phase 3 study. Lancet. 2023;402:1133–46. https://doi.org/10.1016/S0140-6736(23)00961-3.
9. Anwanwan D, Singh SK, Singh S, Saikam V, Singh R. Challenges in liver cancer and possible treatment approaches. Biochim Biophys Acta (BBA) Rev Cancer. 2020;1873: 188314. https://doi.org/10.1016/j.bbcan.2019.188314.
10. Yang X, Yang C, Zhang S, Geng H, Zhu AX, Bernards R, et al. Precision treatment in advanced hepatocellular carcinoma. Cancer Cell. 2024;42:180–97. https://doi.org/10.1016/j.ccell.2024.01.007.
11. Guerrero Llobet S, Bhattacharya A, Everts M, Kok K, van der Vegt B, Fehrmann RSN, et al. An mRNA expression-based signature for oncogene-induced replication-stress. Oncogene. 2022;41:1216–24. https://doi.org/10.1038/s41388-021-02162-0.
12. Reddy RB, Khora SS, Suresh A. Molecular prognosticators in clinically and pathologically distinct cohorts of head and neck squamous cell carcinoma-a meta-analysis approach. PLoS One. 2019;14:e0218989. https://doi.org/10.1371/journal.pone.0218989.
13. Gao M, Liu W, Li T, Song Z, Wang X, Zhang X. Identifying genetic signatures associated with oncogene-induced replication stress in osteosarcoma and screening for potential targeted drugs. Biochem Genet. 2023;62:1690–715. https://doi.org/10.1007/s10528-023-10497-4.
14. Xu W, Rao Q, An Y, Li M, Zhang Z. Identification of biomarkers for barcelona clinic liver cancer staging and overall survival of patients with hepatocellular carcinoma. PLoS One. 2018;13:e0202763. https://doi.org/10.1371/journal.pone.0202763.
15. Shao P, Sun D, Wang L, Fan R, Gao Z. Deep sequencing and comprehensive expression analysis identifies several molecules potentially related to human poorly differentiated hepatocellular carcinoma. FEBS Open Bio. 2017;7:1696–706. https://doi.org/10.1002/2211-5463.12310.
16. Yu Y, Li Y, Zhou L, Cheng X, Gong Z. Hepatic stellate cells promote hepatocellular carcinoma development by regulating histone lactylation: novel insights from single-cell RNA sequencing and spatial transcriptomics analyses. Cancer Lett. 2024;604:217243. https://doi.org/10.1016/j.canlet.2024.217243.
17. Wang F, Long J, Li L, Wu Z-X, Da T-T, Wang X-Q, et al. Single-cell and spatial transcriptome analysis reveals the cellular heterogeneity of liver metastatic colorectal cancer. Sci Adv. 2023;9:eadf5464. https://doi.org/10.1126/sciadv.adf5464.
18. Uhlen M, Zhang C, Lee S, Sjöstedt E, Fagerberg L, Bidkhori G, et al. A pathology atlas of the human cancer transcriptome. Science. 2017;357:eaan2507. https://doi.org/10.1126/science.aan2507.
19. Robin X, Turck N, Hainard A, Tiberti N, Lisacek F, Sanchez J-C, et al. pROC: an open-source package for R and S + to analyze and compare ROC curves. BMC Bioinformatics. 2011;12:77. https://doi.org/10.1186/1471-2105-12-77.
20. Wang Y, Backman TWH, Horan K, Girke T. fmcsR: mismatch tolerant maximum common substructure searching in R. Bioinformatics. 2013;29:2792–4. https://doi.org/10.1093/bioinformatics/btt475.
21. Newman AM, Steen CB, Liu CL, Gentles AJ, Chaudhuri AA, Scherer F, et al. Determining cell type abundance and expression from bulk tissues with digital cytometry. Nat Biotechnol. 2019;37:773–82. https://doi.org/10.1038/s41587-019-0114-2.
22. Hao Y, Hao S, Andersen-Nissen E, Mauck WM, Zheng S, Butler A, et al. Integrated analysis of multimodal single-cell data. Cell. 2021;184:3573-3587.e29. https://doi.org/10.1016/j.cell.2021.04.048.
23. Korsunsky I, Millard N, Fan J, Slowikowski K, Zhang F, Wei K, et al. Fast, sensitive and accurate integration of single-cell data with harmony. Nat Methods. 2019;16:1289–96. https://doi.org/10.1038/s41592-019-0619-0.
24. Zappia L, Oshlack A. Clustering trees: a visualization for evaluating clusterings at multiple resolutions. Gigascience. 2018;7:giy083. https://doi.org/10.1093/gigascience/giy083.
25. Ianevski A, Giri AK, Aittokallio T. Fully-automated and ultra-fast cell-type identification using specific marker combinations from single-cell transcriptomic data. Nat Commun. 2022;13:1246. https://doi.org/10.1038/s41467-022-28803-w.
26. Quan F, Liang X, Cheng M, Yang H, Liu K, He S, et al. Annotation of cell types (ACT): a convenient web server for cell type annotation. Genome Med. 2023;15:91. https://doi.org/10.1186/s13073-023-01249-5.
27. Timothy T, Itay T, Christophe G et al. inferCNV Trinity CTAT Project. 2019. https://github.com/broadinstitute/inferCNVA
28. Wu H, Gonzalez Villalobos R, Yao X, Reilly D, Chen T, Rankin M, et al. Mapping the single-cell transcriptomic response of murine diabetic kidney disease to therapies. Cell Metab. 2022;34:1064-1078.e6. https://doi.org/10.1016/j.cmet.2022.05.010.
29. Wu T, Hu E, Xu S, Chen M, Guo P, Dai Z, et al. clusterProfiler 4.0: a universal enrichment tool for interpreting omics data. Innovation (Camb). 2021;2:100141. https://doi.org/10.1016/j.xinn.2021.100141.
30. Hänzelmann S, Castelo R, Guinney J. GSVA: gene set variation analysis for microarray and RNA-seq data. BMC Bioinformatics. 2013;14:7. https://doi.org/10.1186/1471-2105-14-7.
31. Trapnell C, Cacchiarelli D, Grimsby J, Pokharel P, Li S, Morse M, et al. The dynamics and regulators of cell fate decisions are revealed by pseudotemporal ordering of single cells. Nat Biotechnol. 2014;32:381–6. https://doi.org/10.1038/nbt.2859.
32. Jun Z, ClusterGVis. One-step to cluster and visualize gene expression data. 2025. https://github.com/junjunlab/ClusterGVis
33. Jin S, Guerrero-Juarez CF, Zhang L, Chang I, Ramos R, Kuan C-H, et al. Inference and analysis of cell-cell communication using CellChat. Nat Commun. 2021;12:1088. https://doi.org/10.1038/s41467-021-21246-9.

34. Kueckelhaus J, Frerich S, Kada-Benotmane J, Koupourtidou C, Ninkovic J, Dichgans M, et al. Inferring histology-associated gene expression gradients in spatial transcriptomic studies. Nat Commun. 2024;15:7280. https://doi.org/10.1038/s41467-024-50904-x.
35. Zhan L, Luo X, Xie W, Zhu X-A, Xie Z, Lin J, et al. Shinytempsignal: an R shiny application for exploring temporal and other phylogenetic signals. J Genet Genomics. 2024;51:762–8. https://doi.org/10.1016/j.jgg.2024.02.004.
36. Hwang SY, Danpanichkul P, Agopian V, Mehta N, Parikh ND, Abou-Alfa GK, et al. Hepatocellular carcinoma: updates on epidemiology, surveillance, diagnosis and treatment. Clin Mol Hepatol. 2025;31:S228-54. https://doi.org/10.3350/cmh.2024.0824.
37. Ershov P, Yablokov E, Mezentsev Y, Ivanov A, Multidisciplinary Digital Publishing Institute. Uncharacterized proteins CxORFx: subinteractome analysis and prognostic significance in cancers. Int J Mol Sci. 2023;24:10190. https://doi.org/10.3390/ijms241210190.
38. Bishara LA, Abu-Zhayia ER, Nicola M, Ayoub N. C8orf33 dictates DNA double-strand break repair choice by modulating KAT8-mediated H4K16 acetylation. Cell Death Dis. 2025;16:834. https://doi.org/10.1038/s41419-025-08194-8.
39. Wu Y, Zhou L, Zou Y, Zhang Y, Zhang M, Xu L, et al. Disrupting the phase separation of KAT8-IRF1 diminishes PD-L1 expression and promotes antitumor immunity. Nat Cancer. 2023;4:382–400. https://doi.org/10.1038/s43018-023-00522-1.
40. Bi S, Huang L, Chen Y, Hu Z, Li S, Wang Y, et al. KAT8-mediated H4K16ac is essential for sustaining trophoblast self-renewal and proliferation via regulating CDX2. Nat Commun. 2024;15:5602. https://doi.org/10.1038/s41467-024-49930-6.
41. Pal D, Patel M, Boulet F, Sundarraj J, Grant OA, Branco MR, et al. H4K16ac activates the transcription of transposable elements and contributes to their cis-regulatory function. Nat Struct Mol Biol. 2023;30:935–47. https://doi.org/10.1038/s41594-023-01016-5.
42. Liu Y, Sigova A, O'Donnell CW, Smith C, Whissell G, Chevalier B et al. Identification and targeted modulation of gene signaling networks. 2018. https://patents.google.com/patent/WO2018204764A1/en. Accessed 11 Feb 2026.
43. Monasso GS, Hoang TT, Mancano G, Fernández-Barrés S, Dou J, Jaddoe VWV, et al. A meta-analysis of epigenome-wide association studies on pregnancy vitamin B12 concentrations and offspring DNA methylation. Epigenetics. 2023;18:2202835. https://doi.org/10.1080/15592294.2023.2202835.
44. Zhu Z, Mallik S, Stevens TA, Huang R, Levy ED, Shan S. Principles of cotranslational mitochondrial protein import. Cell. 2025;188:5605-5617.e14. https://doi.org/10.1016/j.cell.2025.07.021.
45. Zhou X, Liao W-J, Liao J-M, Liao P, Lu H. Ribosomal proteins: functions beyond the ribosome. J Mol Cell Biol. 2015;7:92–104. https://doi.org/10.1093/jmcb/mjv014.
46. Boulon S, Westman BJ, Hutten S, Boisvert F-M, Lamond AI. The nucleolus under stress. Mol Cell. 2010;40:216–27. https://doi.org/10.1016/j.molcel.2010.09.024.
47. Zhu G-Q, Tang Z, Huang R, Qu W-F, Fang Y, Yang R, et al. CD36 + cancer-associated fibroblasts provide immunosuppressive microenvironment for hepatocellular carcinoma via secretion of macrophage migration inhibitory factor. Cell Discov. 2023;9:25. https://doi.org/10.1038/s41421-023-00529-z.
48. Liu F, Li X, Zhang Y, Ge S, Shi Z, Liu Q, et al. Targeting tumor-associated macrophages to overcome immune checkpoint inhibitor resistance in hepatocellular carcinoma. J Exp Clin Cancer Res. 2025;44:227. https://doi.org/10.1186/s13046-025-03490-9.
49. Figueiredo CR, Azevedo RA, Mousdell S, Resende-Lara PT, Ireland L, Santos A, et al. Blockade of MIF-CD74 signalling on macrophages and dendritic cells restores the antitumour immune response against metastatic melanoma. Front Immunol. 2018;9:1132. https://doi.org/10.3389/fimmu.2018.01132.
50. Llovet JM, Pinyol R, Yarchoan M, Singal AG, Marron TU, Schwartz M, et al. Adjuvant and neoadjuvant immunotherapies in hepatocellular carcinoma. Nat Rev Clin Oncol. 2024;21:294–311. https://doi.org/10.1038/s41571-024-00868-0.

Publisher's Note